Prediction of high-strain polar phases in antiferroelectric $PbZrO_3$ from a multiscale approach

S. Lisenkov,[1] Yulian Yao,[2] Nazanin Bassiri-Gharb,[2,3] and I. Ponomareva[1,*]
[1]*Department of Physics, University of South Florida, Tampa, Florida 33620, USA*
[2]*School of Materials Science and Engineering, Georgia Institute of Technology, Atlanta, Georgia 30332, USA*
[3]*G. W. Woodruff School of Mechanical Engineering, Georgia Institute of Technology, Atlanta, Georgia 30313, USA*

(Received 6 July 2020; revised 14 August 2020; accepted 24 August 2020; published 8 September 2020)

$PbZrO_3$ is regarded as the first antiferroelectric and currently is under intense reexamination. We propose a multiscale approach that combines classical and first-principles density functional theory based simulations to explore polar phases in this material. Application of this approach to $PbZrO_3$ predicts three polar phases, none of which is the common $R3c$. The lowest-energy polar phase Cc is metastable at 0 K but can be stabilized by application of electric field. Its structural and polarization response to the electric field is in good agreement with experimental data from the literature. The other two phases are $Ima2$ and $I4cm$ of orthorhombic and tetragonal symmetry, respectively, and predicted to stabilize at finite temperatures and under application of larger electric fields. These two phases exhibit very large strain which is of technological significance.

DOI: 10.1103/PhysRevB.102.104101

I. INTRODUCTION

$PbZrO_3$ is the archetypical antiferroelectric perovskite whose properties have been investigated since 1950s. In fact, it is regarded as the first known antiferroelectic [1]. Antiferroelectrics are the antipolar counterparts of ferroelectrics that do not exhibit spontaneous polarization. They are defined by the presence of polar metastable phase(s) close in energy to the equilibrium antipolar phase so that the transition between the two is possible by the application of an electric field [2]. This energetic proximity of the polar and antipolar phases gives origin to the famous double-loop structure for the electric hysteresis in antiferroelectrics. For $PbZrO_3$ it has been well established both experimentally and computationally that such polar phase is $R3c$ [3–5], quite independent of the direction of the applied electric field [3,6,7]. But, is this the only polar metastable phase of $PbZrO_3$? The dominance of the $R3c$ phase seems like a strong evidence for its reigning status. Could this dominance be just the consequence of the energetic proximity of $R3c$ to the equilibrium antipolar $Pbam$ phase? Could there still be some overlooked metastable polar phases? Interestingly, despite $PbZrO_3$ archetypical antiferroelectric status, the longest in the history of antiferroelectrics' investigation, and the recent reexamination wave [2,8–11], this question has not received much attention. One of the possible reasons for the dearth of work in this field is the stability of the $Pbam$ structure, making it difficult to observe double hysteresis loops at room temperature [1,12]. For example, for $PbZrO_3$ ceramics the coercive field is larger than its dielectric breakdown strength. This challenge can be overcome with high-quality $PbZrO_3$ single crystals or thin films [13]. Experimentally, the temperature-electric field phase diagram was studied in single-crystal $PbZrO_3$ in Ref. [14]. Application of the electric field up to 1400 kV/cm was shown to induce multiple phase transitions. For example, "sixfold" hysteresis loops corresponding to three phase transitions have been observed around room temperature. The transitions are from antiferroelectric orthorhombic $Pba2$ to ferroelectric orhorhombic $C2mm$ (≈220 kV/cm) to ferroelectric rhombohedral probably $R3m$ (≈330 kV/cm) to ferroelectric rhombohedral probably $R3c$ (≈400 kV/cm) phases when the field was applied along $[210]_O$. However, when the field was applied along $[001]_O$ (although in a different temperature range) a single transition from antiferroelectric $Pba2$ to ferroelectric probably $R3m$ occurred. The study revealed the possibility of several metastable polar phases whose appearance depends on both temperature and the direction of the electric field. On the other hand, no sixfold loops have been observed in $PbZrO_3$ films study under application of fields up to 500 kV/cm [15]. Instead a single transition (twofold loops) into rhombohedral phase with $[111]_T$ polarization direction was observed. Similarly, only double loops were observed in another experimental study on $PbZrO_3$ films [7]. In Ref. [3] the possibility of low-coercive field phase with the polarization direction along the c axis in $PbZrO_3$ thin films was proposed.

The lack of computational insight into the question of polar phases in $PbZrO_3$ is rather stunning since the search and predictions of metastable phases are the "holy grail" of computations. Early density functional theory (DFT) computational studies were instrumental in identifying $R3c$ as the energetically closest polar phase to $Pbam$ [4,5]. In Ref. [4] the polar $Pba2$ phase was found to be 0.02 eV higher in energy than $R3c$. In Ref. [16] freezing-in the polar unstable modes of cubic $PbZrO_3$ resulted in $BaTiO_3$-like hypothetical $P4mm$, $Amm2$, and $R3m$ polar phases. The latter one leads to the metastable $R3c$ once the oxygen octahedra rotations are added. The possibility to stabilize a polar orthorhombic phase by application of very large electric field up to 4 MV/cm was proposed by some of us in Ref. [17]. So, it appears that the computational and experimental evidence this far suggest that if metastable polar phases other than $R3c$ for $PbZrO_3$ do exist they are likely to be much higher in energy and, therefore,

*iponomar@usf.edu

 ©2020 American Physical Society

require high stabilizing electric field. While large electric fields are challenging experimentally, computational investigation offers an excellent tool to overcome this challenge and provide a valuable insight. Therefore, in this study we aim (i) to design a multiscale first-principles computational approach for predictions of polar phases; (ii) to apply this approach to predict previously overlooked polar phases of $PbZrO_3$; (iii) to validate some of our computational predictions by comparison with experimental data from the literature; (iv) to propose an experimental route to induce such polar phases through an application of electric fields.

II. METHODOLOGY

To achieve our aims, we combined the first-principles-based effective Hamiltonian approach with first-principles DFT simulations. The effective Hamiltonian is used to study $PbZrO_3$ at finite temperatures, however, it does not allow for structural relaxation which may compromise its quantitative predictions. On the other hand, DFT simulations provide the highest accuracy but are limited to 0 K for most practical purposes. For the effective Hamiltonian simulations we used a supercell made of $16 \times 16 \times 16$ unit cells of cubic perovskite with periodic boundary conditions applied along all three Cartesian directions to model bulk. The energy of the supercell is given by the first-principles-based effective Hamiltonian of Ref. [17]. The degrees of freedom for the effective Hamiltonian include polar local modes $\mathbf{u}_i$, which are proportional to the local dipole moment in the unit cell i and describe the antiferroelectric instability at Σ_2 point of the Brillouin zone, antiferrodistortive local modes $\mathbf{w}_i$ that describe oxygen octahedra tilts about Cartesian axes and are responsible for the R_4 point instability, and inhomogeneous and homogeneous strain variables, which describe elastic deformations of the unit cell and supercell, respectively. The Hamiltonian includes energy associated with the antiferroelectric Σ_2 mode and contains contributions from the dipole-dipole interactions, short-range interactions, and onsite self-energy. It also includes energy due to the antiferrodistortive mode that is similar to the previous one but excludes the dipole-dipole interactions as antiferrodistortive local modes are nonpolar. Finally, the Hamiltonian includes the energy associated with elastic deformations. All degrees of freedom are coupled with each other by the symmetry-allowed interactions. Simulation of an external electric field is achieved by adding a term to the effective Hamiltonian that couples electric dipoles with the electric field. All parameters of the effective Hamiltonian are derived local density approximation (LDA) DFT calculations [17]. This Hamiltonian correctly reproduces the sequence of phase transition in $PbZrO_3$, its electrical properties, behavior under pressure [17], and mode dynamics [18]. It has previously been used to simulate both bulk and low-dimensional $PbZrO_3$ structures and in both static and dynamic settings [11,17–19]. In this work, the Hamiltonian was used in the framework of Metropolis Monte Carlo (MC) simulations to simulate canonical ensemble.

DFT simulations were performed using the Vienna *ab initio* simulation package (VASP) [20] with the projector-augmented wave method [21,22]. LDA was used as the exchange-correlation functional [23]. An energy cutoff of 600 eV was used to truncate a plane-wave basis. We used Γ-centered k-point mesh with spacing of 0.3 $Å^{-1}$ in our calculations. Calculations with the energy cutoff 1000 eV and 0.15 $Å^{-1}$ k-point spacing for cubic $PbZrO_3$ yielded 15 meV/f.u. difference in energy which can be used as the computational error. The relaxations were performed until forces were less than 5 meV/Å. The spontaneous polarization is calculated according to the modern theory of polarization [24–26]. The space groups for the phases were identified and distortion paths constructed using ISOTROPY suite [27,28] with its default settings in most of the cases.

III. RESULTS AND DISCUSSION

A. Finite-temperature predictions from effective Hamiltonian simulations

We begin with investigation of the equilibrium phases in $PbZrO_3$ under applied electric fields of different direction. The simulated sample was also subjected to annealing in the presence of electric field of different orientations. Four different directions of the electric field have been investigated, $[001]_C$, $[110]_C$, $[111]_C$, and $[021]_C$ in the direction of cubic perovskite. The following electric fields were simulated: 1.0, 1.2, 1.4, 1.6, 1,8, 2.0, 3.0, 4.0, and 5.0 MV/cm. Annealing started at the temperature of 695 K and continued in steps of 5 K until the temperature reached 295 K. Note that we report temperatures that have been rescaled with the factor 1.87 from the simulation values to match the experimental Curie temperature. For each temperature step we simulated 500 000 MC steps, 250 000 of which were used for equilibration and 250 000 were used for averaging. We collected the average polarization, antiferroelectric order parameter, strain, and antiferrodistortive order parameter associated with the oxygen octahedra tilts. The computations yielded the dependence of the aforementioned order parameters on temperature and electric field vector. These data were used to compute the phase diagrams which give the dependence of the Curie temperature on the electric field. These diagrams are given in Fig. 1. For each direction of the electric field we find a single transition from antipolar to polar phase within the chosen computational resolution for the electric field. The direction of the polarization in the polar phase is indicated on the diagrams. In all cases our simulations predict that at equilibrium the direction of the polarization coincides with the direction of the electric field, which suggests the possibility of stabilizing several polar phases in $PbZrO_3$. Another interesting observation from the phase diagrams is that the magnitude of the electric field that induces the polar phase depends on the field direction. For example, the effective Hamiltonian predicts that at room temperature the smallest electric field is required to induce the polar phase with polarization along either $[111]_C$ or $[001]_C$ direction.

B. DFT insight

Next, we investigate the polar phases predicted by the effective Hamiltonian using DFT simulations. Technically, we pick one representative polar structure from each part of the phase diagrams in Fig. 1 and reduce its supercell to the smallest size consistent with the order parameters values obtained in the finite-temperature simulations. These reduced

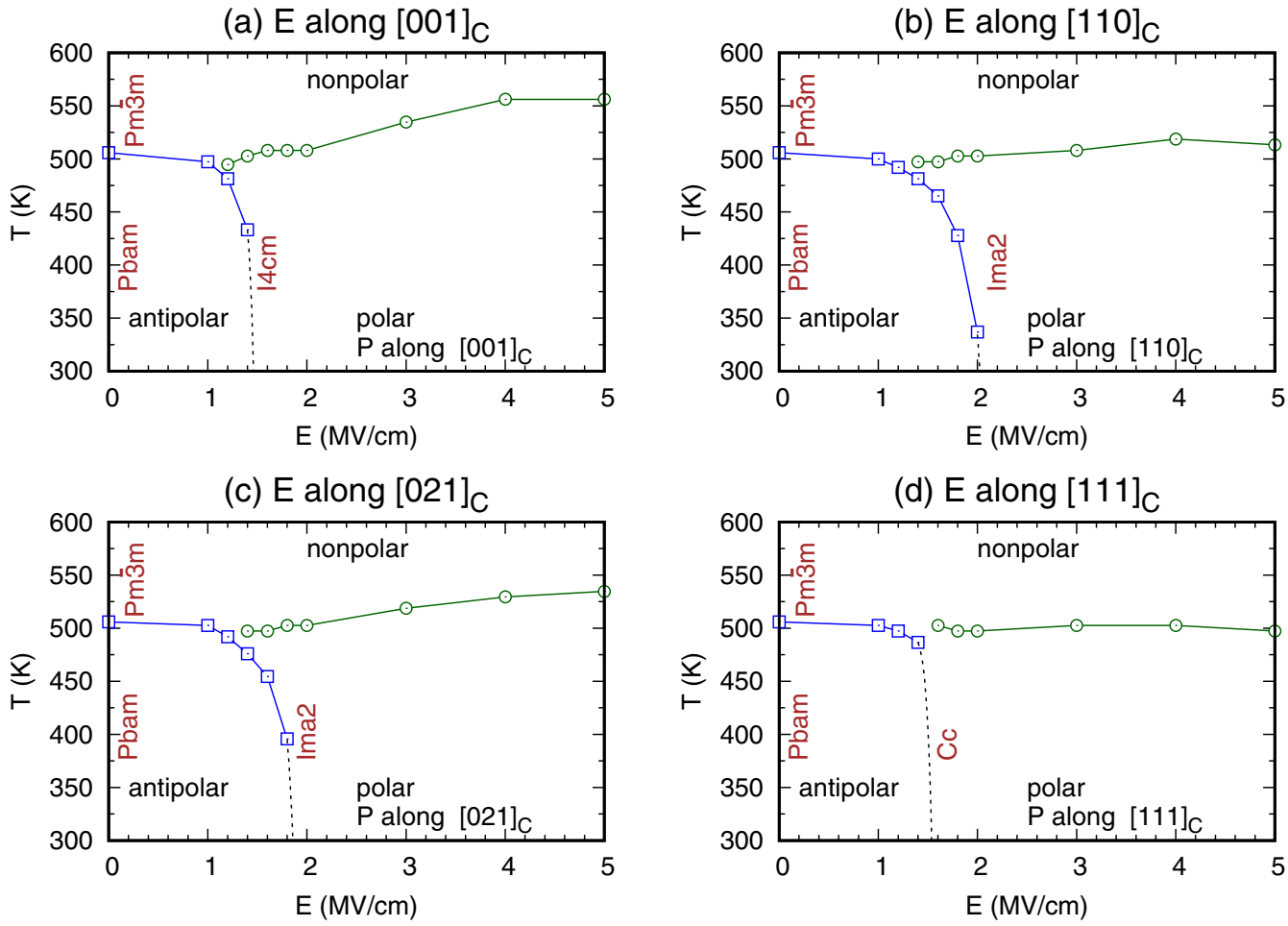

FIG. 1. Phase diagram for the dependence of the Curie temperature on the applied electric field. Different panels correspond to the different direction of the field application as given in the titles. Space groups indicated in maroon correspond to fully relaxed structures in DFT simulations without electric field.

supercells are first subjected to ionic relaxation using DFT while keeping the shape and size of the supercell fixed. Table I (upper part) gives structural parameters, polarizations, and energy with respect to the ground state (*Pbam*) for different phases obtained in such simulations. *R*3*c* is the lowest-energy polar phase and has the largest polarization.

TABLE I. Structural parameters, energy with respect to the ground state, and polarization for the polar phases found in DFT simulations along with the ground state *Pbam* and cubic $Pm\bar{3}m$ phases. The letters in parentheses state the obtained crystal system: monoclinic (M), orthorhombic (O), rhombohedral (R), and tetragonal (T).

Phase	Ionic relaxation only a,b,c (Å)	α, β, γ (degrees)	V (Å^3)	E (meV/f.u.)	P_s (μC/cm^2)
*R*3*c* (R)	5.78, 5.78, 5.78	60, 60, 60	137	8	52
*Ima*2 (O)	8.13, 5.83, 5.80	90, 90, 90	275	19	53
Cm (M)	8.12, 8.12, 5.81	90, 134, 90	275	26	35
*Iba*2 (O)	5.89, 5.81, 8.15	90, 90, 90	278	126	42
	Full structural relaxation				
Pbam (O)	5.81, 11.70, 8.11	90, 90, 90	551	0	0
Cc (M)	10.05, 5.80, 5.81	90, 125, 90	277	5	58
*Ima*2 (O)	8.11, 5.85, 5.84	90, 90, 90	277	15	56
*I*4*cm* (T)	5.73, 5.73, 8.40	90, 90, 90	276	63	48
$Pm\bar{3}m$ (C)	4.11, 4.11, 4.11	90, 90, 90	70	316	0

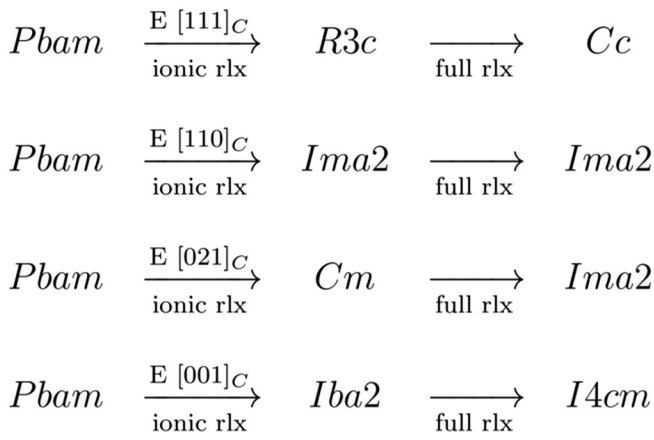

FIG. 2. Sequence of the phase evolution in multiscale structure prediction.

Next, full structural relaxation of the phases reported in the upper part of Table I was carried out and the data are added to the same table (bottom part). Figure 2 gives the sequence of phase evolution in such multiscale structure prediction. Each sequence starts with *Pbam* in effective Hamiltonian simulations then transitions into one of the polar phases under application of the electric field in effective Hamiltonian simulations followed by ionic relaxation using DFT. The last step of the sequence is the polar phase obtained after full structural relaxation in DFT. Interestingly, we find that the *R*3*c* phase transforms into *Cc* phase after full structural relaxation as determined by ISOTROPY [27] within the default tolerance of 10^{-5} for the lattice parameters. Increasing the tolerance to 4×10^{-5} results in identifying the supercell space group as *R*3*c*, while decreasing the tolerance by orders of magnitude with respect to default value preserves *Cc*. The small energy difference between *R*3*c* and *Cc* structures (3 meV/f.u.) is within our computational accuracy and raises the question whether the phase ordering can be affected by the computational settings. To address this, we first note that both structures were simulated with the 10-atoms supercells, the same *k*-points mesh, and same energy cutoff so the systematic errors are canceled. Second, we carried out additional simulations to estimate the role of the exchange-correlation functional. In particular, full structural relaxation of both *R*3*c* and *Cc* using PBE [29] functional predicted that *Cc* phase is still lower in energy but only by 0.014 meV/f.u. We have also computed the energies for both LDA predicted structures using HSE06 [30] hybrid functional and found that the *R*3*c* structure is 0.9 meV/f.u. lower in energy than *Cc*. Such a small energy difference does not allow for drawing any conclusion without full structural relaxation, which we could not carry out due to the computationally demanding nature of the HSE06 functional. Note that a recent investigation into functional performance assessment on prototypical ferroelectrics revealed that despite its simplicity, LDA is still among the best performers [31]. Third, we looked at the dynamical stability of both structures and found both of them dynamically stable, that is, neither phase exhibited imaginary frequencies. On the basis of this investigation we conclude that the *Cc* phase is the ground state at least within the chosen computational scheme. At the same time, the energetic proximity of the *R*3*c* and *Cc* phases and their small structural difference suggests that they both can occur at finite temperatures and are even likely to be indistinguishable experimentally. The *Cc* phase is the closest to the ground state in energy and only 5 meV/f.u. higher in energy. Although, it should be noted that LDA calculations typically underestimate the energy differences between phases in ferroelectrics. *Cc* also has the largest polarization among the predicted polar phases which agrees well with the previously reported experimental room-temperature value of 40 μC/cm^2 [7].

Next to *Cc* in energy and polarization is the orthorhombic *Ima*2 phase. However, *Ima*2 is about three times higher in energy than *Cc*, which suggests that its stabilization requires very large electric field. The *Cm* phase that originated from $[021]_C$ direction of the electric field converged to *Ima*2 after full relaxation. Finally, the polar phase with the highest energy is of tetragonal symmetry (*I*4*cm*). It has the lowest polarization and is 14 times higher in energy than the *Cc* phase. We also computed phonon frequencies for the fully relaxed phases.

The lowest-energy *Cc* phase has no unstable modes, while the other two polar phases have unstable phonons. Further relaxation of their supercells slightly distorted along the direction of the unstable modes converged to the *Cc* phase. These computations suggest that at 0 K the *Cc* is the only metastable phase of $PbZrO_3$. However, the other two polar phases are likely to become metastable at higher temperatures just like tetragonal and orthorhombic phases of $BaTiO_3$ that are unstable at 0 K but are stabilized at finite temperatures. This hypothesis is also supported by the following: (i) these phases are still energetically more favorable than $Pm\bar{3}m$ that is stable above the Curie temperature; and (ii) they originated from the phases that are stable at finite temperatures in effective Hamiltonian simulations. Finite-temperature DFT molecular dynamics could be employed to further confirm phase stability.

To gain insight into the transition from the antipolar to these polar phases we constructed a distortion path between the ground state and each of the polar phases. The energy, polarization, and strain were calculated along the distortion path and used to obtain the energy and strain dependence on the polarization. The data are given in Fig. 3. Note that the strain difference is reported along the direction of polarization and, therefore, the direction of the applied electric field. Figure 3(a) demonstrates that the three polar phases are associated with local minima in the energy profile along the polar direction. The presence of the energy barriers predicts the electric hysteresis that indeed is observed in our effective Hamiltonian simulations. The structure of the energy curves resembles those of $BaTiO_3$. The data for the points associated with minimum in energy are also reported in Table II.

Figure 3(b) shows that a large strain change is associated with a transition into one of the polar phases. The strain in those points are 0.006, 0.010, and 0.036 for *Cc*, *Ima*2, and *I*4*cm* phases, respectively (see η_{polar} in Table II). The value for *Cc* phase agrees well with the experimentally reported 0.0064–0.0068 for (111)-oriented $PbZrO_3$ films [32]. The strain associated with *I*4*cm*, however, is ginormous, far exceeding both *Cc* and *Ima*2 values. In fact, it is six times larger than the one due to the transition into the *Cc* phase. We

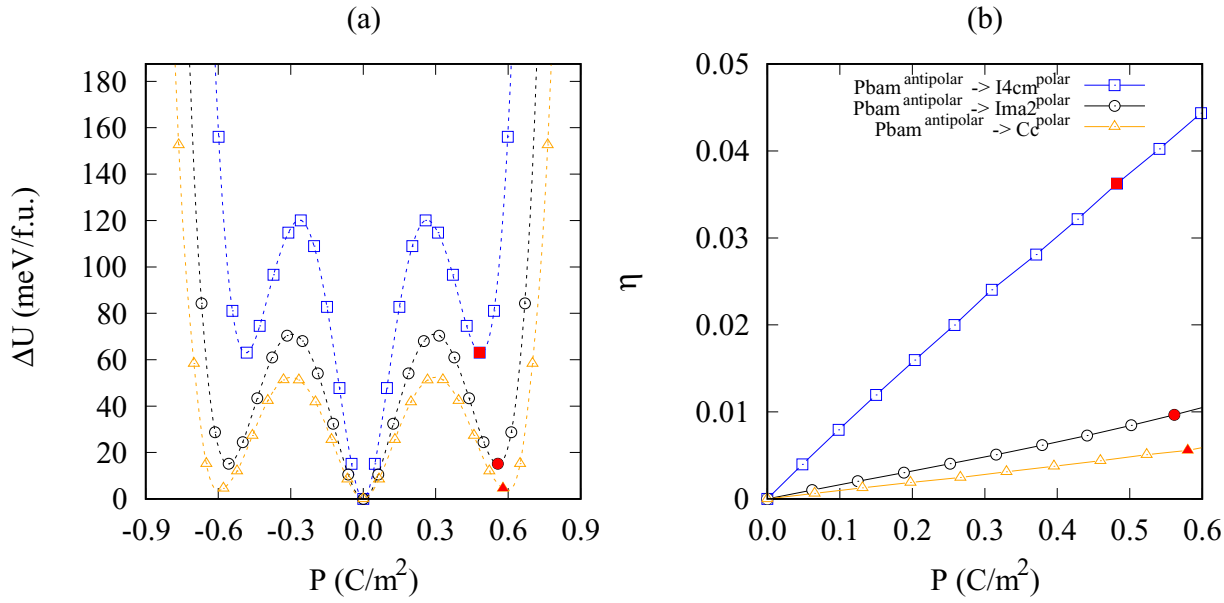

FIG. 3. Dependence of the energy (a) and strain (b) on polarization. Points associated with the local energy minima are marked with red.

believe that this huge difference in strain is responsible for the large energy penalty associated with this phase.

We have also computed strain components with respect to the orthorhombic axes of antiferroelectric *Pbam* and reported them in Table II. For *Cc* phase the largest strain component is $\eta_3 = 0.013$ which is along the $[001]_O$ direction and agrees well with experimental value of 0.011 for (001)-oriented films [33]. From the table we can find that distortion from rhombohedral to the monoclinic symmetry for the lowest-energy phase is associated with a about 3% reduction in the polarization component along the *c* direction. For the other two polar phases, the largest strain is also along the *c* direction and far exceeds the values for the *Cc* phase.

Our predicted phases could hold significant technological potential for piezoelectric applications if they can be induced by an electric field. To explore this possibility, we estimate the electric field associated with the phase coexistence between the *Pbam* phase and each of the polar phases. The common tangent approach similar to the one used to obtain pressure associated with phase coexistence [34] is applied. To derive such an approach in our case we start with the zero-temperature free energy of the supercell, or the enthalpy $G = U(P)/V - PE$, where V is the supercell volume. At equilibrium in a field E the Gibbs free energy is minimized with respect to polarization yielding the equation of state $E = \frac{1}{V}\frac{\partial U}{\partial P}$. Two phases whose (P, U) lie on the common tangent line are associated with the same E. They can coexist if their free energies are equal, that is, $U_1/V - P_1E_{\text{coex}} = U_2/V - P_2E_{\text{coex}}$ yielding $E_{\text{coex}} = \frac{1}{V}\frac{U_2-U_1}{P_2-P_1}$, where (P_1, U_1) and (P_2, U_2) are the points of the common tangent near the global and local minima on the $U(P)$ curve. The values for E_{coex} are listed in Table II. On the electric hysteresis loop the coexistence field is between the two coercive fields associated with the antipolar-polar and polar-antipolar transitions. For the *Cc* phase the coexistence field is 182 kV/cm, which is rather close to the experimental range for phases' coexistence [280:430] kV/cm [7], especially when noting that the experimental values are likely to be larger due to the presence of the depolarizing field. For *Ima*2 phase the coexistence field is 631 kV/cm, which is within the range of experimentally accessible fields [7,14]. Our *Ima*2 could be compared to the *C*2*mm* phase of Ref. [14], which was found to be stable in the range of electric fields above 200 kV/cm (and likely below 800 kV/cm) at temperatures below 150° C. For *I*4*cm* the coexistence field is very large, 3030 kV/cm, and is likely to exceed the dielectric breakdown field for most experimental samples. The largest field applied to $PbZrO_3$ to the best of our knowledge is 1400 kV/cm [14] for single crystals, and 1700 kV/cm for thin films [7], while breakdown field is 2800 kV/cm [33]. At the same time, given the large strain associated with this phase, it is likely that the

TABLE II. Strain and polarization components for the polar phases and the phase coexistence field. η_{polar} reports the strain along the polar direction, while η_1–η_6 give strain along the axes of orthorhombic *Pbam*. Polarization components are reported in the directions of orthorhombic $PbZrO_3$.

Phase	η_{polar}	η_1	η_2	η_3	η_4	η_5	η_6	**P** (μC/cm^2)	E_{coex} (kV/cm)
Cc	0.006	0.000	−0.008	0.013	0.000	0.030	0.000	(0.48,0.00,0.33)	182
*Ima*2	0.010	−0.004	−0.011	0.020	0.001	−0.001	-0.019	(−0.28,0.28,−0.39)	631
*I*4*cm*	0.036	−0.014	−0.020	0.036	0.000	0.000	0.000	(0.00,0.00,-0.48)	3036

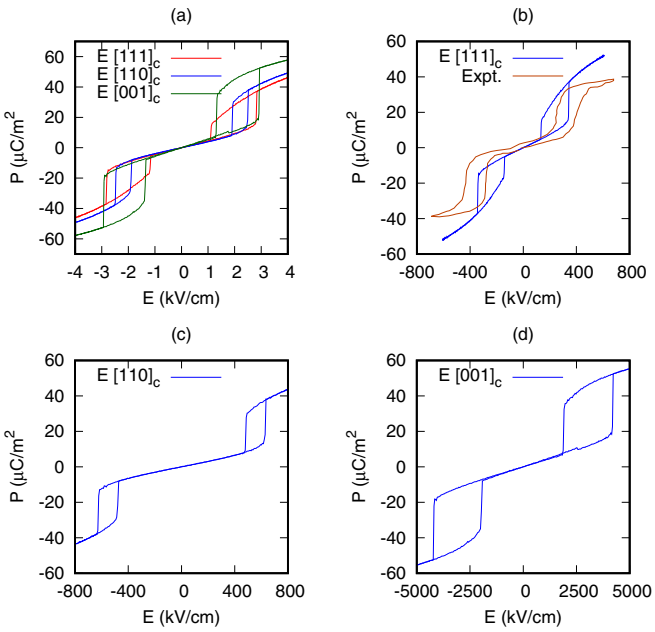

FIG. 4. Room-temperature hysteresis loops computed for different directions of the applied electric field. (a) Shows unrescaled data from the effective Hamiltonian calculations. (b)–(d) Shows the same data but after rescaling has been applied as indicated in the text. In (b) experimental data are taken from Ref. [7].

coexistence field can be tuned by the epitaxial strain offering the possibility of stabilizing this phase.

C. Merging quantum and classical insights

Next, we extend our multiscale computational approach to study room-temperature hysteresis loops in these films to enable comparison with the experimental results in previous literature reports. The room-temperature and 160-K hysteresis loops were computed for electric fields with the following directions: $[001]_C$, $[110]_C$, and $[111]_C$. The room-temperature data are plotted in Fig. 4(a).

Two points need to be emphasized. First, for the field directions studied in computations two different scenarios exist for antipolar-polar-antipolar phase switching. The more favorable one (scenario I) is associated with the phases where the polar and antipolar vectors are not perpendicular. For the less favorable one (scenario II) the two vectors are perpendicular. The coercive fields for scenario II are twice the one for scenario I. Consequently, in simulations we observe almost exclusively scenario I, except for the initial poling where we can force scenario II. Second, the coercive fields depend on the direction of applied electric fields [Fig. 4(a)]. Let us focus on $[001]_C$ field data. The coercive fields are 2800 and 1160 kV/cm at room temperature (and 4000 and 440 kV/cm at 160 K) in good agreement with DFT coexistence field of 3036 kV/cm (see Table II). Such an agreement suggests that the effective Hamiltonian provides reliable description in this case. From the phase diagrams in Fig. 1 we find that for the lowest reported temperature the coexistence field is 1500 kV/cm, which underestimates the DFT 0-K value. For the $[111]_C$ direction of the electric field the lowest temperature coexistence field from the phase diagram is the same. However, it overestimates drastically the DFT $E_{\text{coex}} = 182$ kV/cm, indicating that in this case significant structural relaxation takes place that is not accounted for in the effective Hamiltonian. To improve quantitative predictions of effective Hamiltonian in this case and enable comparison with experiment we rescale the $[111]_C$ electric fields to match DFT E_{coex}. The rescaled data are given in Fig. 4(b) and compared with the experimental loops from the literature. Similar rescaling procedure was used for the $[110]_C$ electric field data that are given in Fig. 4(c). Figure 4(d) gives the data for the $[001]_C$ which we do not rescale since the effective Hamiltonian provides reasonable predictions in this case. We believe that the computational data presented in Figs. 4(b)–4(d) allow for at least semiquantitative comparison with experiment and will stimulate experimental search for these phases.

IV. CONCLUSIONS

In summary, we have proposed a multiscale computational approach to explore polar phases in ferroics. In such an approach, the phases are first identified in a series of classical finite-temperature simulations on large supercells subjected to an applied electric field. In our case, the first-principles-based effective Hamiltonian is used for such classical simulations. Different directions of the electric field are explored in order to expand the search space. The polar structure supercells obtained in such classical simulation are then reduced to smaller sizes that preserve their symmetry and subjected to full structural relaxation using DFT first-principles simulations. This allows for structural relaxation that may not be available in classical simulations and provides quantitative predictions, that are, however, limited to 0 K. Energy analysis and phonon calculations for the predicted phases are used to classify them as stable, metastable, or unstable at 0 K. In our case of antiferroelectric $PbZrO_3$ we computed the distortion path from the antipolar to each of the polar phases which allows for quick estimate for the electric field at which the polar and antipolar phases coexist. This field can later be used to improve finite-temperature quantitative predictions of the effective Hamiltonian simulations.

For the case of $PbZrO_3$ this approach resulted in three polar phases, none of which has been previously reported, to the best of our knowledge. The lowest-energy phase is *Cc* and metatable at 0 K, while the other two, *Ima*2 and *I*4*cm*, are unstable at 0 K and converge to *Cc*. However, they can be stabilized at finite temperatures as per our effective Hamiltonian predictions. *Cc* phase is the lowest-energy polar phase and in close agreement with experimental data from the literature. It can be induced by relatively low electric fields and is associated with rather large intrinsic strain changes up to 0.013. Interestingly, the other two polar phases are predicted to have even larger strain change associated with electric-field-induced phase transition but also require much larger coercive fields. Stabilization of *Ima*2 phase requires fields as large as 700 kV/cm applied along the $[110]_C$ direction and can produce strain change up to 0.020. The last polar phase, *I*4*cm*, requires an extremely large coercive field,

up to 4000 kV/cm which may not be attainable experimentally. The field-induced phase transition into such polar phase is predicted to produce extremely large strain change of up to 0.036. This unusually high strain could explain the large energy penalty associated with the phase. At the same time, we suggest that there could be ways to tune such phase transition through epitaxial strain, for example. We believe that our study will enable efficient search of polar phases in other ferroics and stimulate experimental search of technologically promising polar phases in $PbZrO_3$.

ACKNOWLEDGMENTS

This work is supported by the U. S. Department of Energy, Office of Basic Energy Sciences, Division of Materials Sciences and Engineering, under Grant No. DE-SC0005245 (S.L. and I.P. computational investigations) and the U. S. National Science Foundation under Grant No. CMMI-1537262 (Y.Y. and N.B.-G. experimental insight and discussions). Computer time was provided by USF Research Computing, sponsored in part by NSF MRI CHE-1531590.

[1] Z. Liu, T. Lu, J. Ye, G. Wang, X. Dong, R. Withers, and Y. Liu, Antiferroelectrics for energy storage applications: A review, Adv. Mater. Technol. **3**, 1800111 (2018).

[2] K. M. Rabe, Antiferroelectricity in oxides: A reexamination, *Functional Metal Oxides* (Wiley, Hoboken, NJ, 2013), Chap. 7, pp. 221–244.

[3] L. Pintilie, K. Boldyreva, M. Alexe, and D. Hesse, Coexistence of ferroelectricity and antiferroelectricity in epitaxial $PbZrO_3$ films with different orientations, J. Appl. Phys. **103**, 024101 (2008).

[4] D. J. Singh, Structure and energetics of antiferroelectric $PbZrO_3$, Phys. Rev. B **52**, 12559 (1995).

[5] R. Kagimura and D. J. Singh, First-principles investigations of elastic properties and energetics of antiferroelectric and ferroelectric phases of $PbZrO_3$, Phys. Rev. B **77**, 104113 (2008).

[6] K. Boldyreva, D. Bao, G. Le Rhun, L. Pintilie, M. Alexe, and D. Hesse, Microstructure and electrical properties of (120)o-oriented and of (001)o-oriented epitaxial antiferroelectric $PbZrO_3$ thin films on (100) $SrTiO_3$ substrates covered with different oxide bottom electrodes, J. Appl. Phys. **102**, 044111 (2007).

[7] M. D. Nguyen, T. T. Trinh, H. T. Dang, and H. N. Vu, Understanding the effects of electric-field-induced phase transition and polarization loop behavior on the energy storage performance of antiferroelectric $PbZrO_3$ thin films, Thin Solid Films **697**, 137794 (2020).

[8] A. Tagantsev, K. Vaideeswaran, S. Vakhrushev, A. Filimonov, R. Burkovsky, A. Shaganov, D. Andronikova, A. Rudskoy, A. Baron, H. Uchiyama, D. Chernyshov, A. Bosak, Z. Ujma, K. Roleder, A. Majchrowski, J.-H. Ko, and N. Setter, The origin of antiferroelectricity in $PbZrO_3$, Nat. Commun. **4**, 3229 (2013).

[9] X.-K. Wei, C.-L. Jia, H.-C. Du, K. Roleder, J. Mayer, and R. E. Dunin-Borkowski, An Unconventional Transient Phase with Cycloidal Order of Polarization in Energy-Storage Antiferroelectric $PbZrO_3$, Adv. Mater. **32**, 1907208 (2020).

[10] J. Hlinka, T. Ostapchuk, E. Buixaderas, C. Kadlec, P. Kuzel, I. Gregora, J. Kroupa, M. Savinov, A. Klic, J. Drahokoupil, I. Etxebarria, and J. Dec, Multiple Soft-Mode Vibrations of Lead Zirconate, Phys. Rev. Lett. **112**, 197601 (2014).

[11] B. K. Mani, C.-M. Chang, S. Lisenkov, and I. Ponomareva, Critical Thickness for Antiferroelectricity in $PbZrO_3$, Phys. Rev. Lett. **115**, 097601 (2015).

[12] X. Tan, C. Ma, J. Frederick, S. Beckman, and K. G. Webber, The antiferroelectric ferroelectric phase transition in lead-containing and lead-free perovskite ceramics, J. Am. Ceramic Soc. **94**, 4091 (2011).

[13] X. Hao, J. Zhai, L. B. Kong, and Z. Xu, A comprehensive review on the progress of lead zirconate-based antiferroelectric materials, Prog. Mater. Sci. **63**, 1 (2014).

[14] O. E. Fesenko, R. V. Kolesova, and Y. G. Sindeyev, The structural phase transitions in lead zirconate in super-high electric fields, Ferroelectrics **20**, 177 (1978).

[15] J. Parui and S. B. Krupanidhi, Slim pe hysteresis loop and anomalous dielectric response in sol-gel derived antiferroelectric $PbZrO_3$ thin films, J. Appl. Phys. **104**, 024107 (2008).

[16] S. E. Reyes-Lillo and K. M. Rabe, Antiferroelectricity and ferroelectricity in epitaxially strained $PbZrO_3$ from first principles, Phys. Rev. B **88**, 180102(R) (2013).

[17] B. K. Mani, S. Lisenkov, and I. Ponomareva, Finite-temperature properties of antiferroelectric $PbZrO_3$ from atomistic simulations, Phys. Rev. B **91**, 134112 (2015).

[18] Z. G. Fthenakis and I. Ponomareva, Dynamics of antiferroelectric phase transition in $PbZrO_3$, Phys. Rev. B **96**, 184110 (2017).

[19] Z. G. Fthenakis and I. Ponomareva, Intrinsic dynamics of the electric-field-induced phase switching in antiferroelectric $PbZrO_3$ ultrathin films, Phys. Rev. B **98**, 054107 (2018).

[20] G. Kresse and J. Furthmüller, Efficient iterative schemes for ab initio total-energy calculations using a plane-wave basis set, Phys. Rev. B **54**, 11169 (1996).

[21] P. E. Blöchl, Projector augmented-wave method, Phys. Rev. B **50**, 17953 (1994).

[22] G. Kresse and D. Joubert, From ultrasoft pseudopotentials to the projector augmented-wave method, Phys. Rev. B **59**, 1758 (1999).

[23] D. M. Ceperley and B. J. Alder, Ground State of the Electron Gas by a Stochastic Method, Phys. Rev. Lett. **45**, 566 (1980).

[24] R. D. King-Smith and D. Vanderbilt, Theory of polarization of crystalline solids, Phys. Rev. B **47**, 1651 (1993).

[25] D. Vanderbilt and R. D. King-Smith, Electric polarization as a bulk quantity and its relation to surface charge, Phys. Rev. B **48**, 4442 (1993).

[26] R. Resta, Macroscopic polarization in crystalline dielectrics: The geometric phase approach, Rev. Mod. Phys. **66**, 899 (1994).

[27] B. J. Campbell, H. T. Stokes, D. E. Tanner, and D. M. Hatch, Isodisplace: An internet tool for exploring structural distortions, J. Appl. Crystallogr. **39**, 607 (2006).

[28] H. T. Stokes and D. M. Hatch, *FINDSYM*: Program for identifying the space-group symmetry of a crystal, J. Appl. Crystallogr. **38**, 237 (2005).

[29] J. P. Perdew, K. Burke, and M. Ernzerhof, Generalized Gradient Approximation Made Simple, Phys. Rev. Lett. **77**, 3865 (1996).

[30] A. V. Krukau, O. A. Vydrov, A. F. Izmaylov, and G. E. Scuseria, Influence of the exchange screening parameter on the performance of screened hybrid functionals, J. Chem. Phys. **125**, 224106 (2006).

[31] M. Kingsland, K. A. Lynch, S. Lisenkov, X. He, and I. Ponomareva, Comparative study of minnesota functionals performance on ferroelectric $BaTiO_3$ and $PbTiO_3$, Phys. Rev. Mater. **4**, 073802 (2020).

[32] H. Maiwa and N. Ichinose, Electrical and electromechanical properties of $PbZrO_3$ thin films prepared by chemical solution deposition, J. Appl. Phys. **40**, 5507 (2001).

[33] M. D. Nguyen and G. Rijnders, Comparative study of piezoelectric response and energy-storage performance in normal ferroelectric, antiferroelectric and relaxor-ferroelectric thin films, Thin Solid Films **697**, 137843 (2020).

[34] A. Mujica, A. Rubio, A. Muñoz, and R. J. Needs, High-pressure phases of group-iv, III–V, and II–VI compounds, Rev. Mod. Phys. **75**, 863 (2003).